# Exploring New Sources of Efficiency in Process-Driven Materials Screening for Post-combustion Carbon Capture

Amir H. Farmahini[a*], Daniel Friedrich[b], Stefano Brandani[a], and Lev Sarkisov[a*]

[a]School of Engineering, Institute of Materials and Processes, The University of Edinburgh, Sanderson Building, EH9 3FB

[b]School of Engineering, Institute for Energy Systems, The University of Edinburgh, Sanderson Building, EH9 3FB

## 1. Force field

References to the crystallographic data used to construct atomistic models of adsorbents materials in addition to the atomic force fields required for performing GCMC simulations are provided in Table S1.

**Table S1:** References to the crystallographic data and force fields used in GCMC simulations

| Material | Crystallographic Data | Force Field for $CO_2$ Adsorption | | Force Field for $N_2$ Adsorption | |
|---|---|---|---|---|---|
| | | LJ / charges (Framework) | LJ / charges ($CO_2$) | LJ / charges (Framework) | LJ / charges ($N_2$) |
| Cu-BTC | Chui et al. (1999)[1] | Yang and Zhong (2006)[2] | TraPPE[3] | Karra and Walton (2008)[4] | TraPPE[3] |
| MOF74-Ni | Lee et al. (2015)[5] | Mercado et al. (2016)[6] | EPM2[7, 8] | UFF[9] | TraPPE[3] |
| Silicalite1(MFI) | Fischer and Bell (2012)[10] | Fischer and Bell (2012)[10] | TraPPE[3] | Fischer and Bell (2012)[10] | TraPPE[3] |
| Zeolite 13X | Olson (1995)[11] | Vujic and Lyubartsev (2016)[12] | EPM2[7, 8] | Vujic and Lyubartsev (2016)[12] | Murthy et al. (1980)[13] |

## 2. Porous frameworks in GCMC simulations

The four materials studied in this paper are assumed to have rigid porous frameworks in GCMC simulations details of which are provided in Table S2.

**Table S2**: Framework parameters of solid adsorbents in GCMC simulation

| Material | lengths of unit cell vectors (Å) | Unit cell angles (degree) | Number of Unit cells per framework | Potential cut-off (Å) |
|---|---|---|---|---|
| Cu-BTC | 26.343 - 26.343 - 26.343 | 90 – 90 – 90 | 2×2×2 | 26.0 |
| MOF74-Ni | 15.165 - 15.157 - 15.157 | 117.743 - 117.799 - 117.806 | 4×4×4 | 12.8 |

| | | | | |
|---|---|---|---|---|
| Silicalite1 | 20.090 - 19.738 - 13.142 | 90 – 90 – 90 | 2×2×3 | 19.0 |
| Zeolite 13X | 25.099 - 25.099 - 25.099 | 90 – 90 – 90 | 2×2×2 | 24.0 |

## 3. Process Simulation

The 4-step VSA-LPP process, its flowsheet and model assumptions are explained in the main article. Here, we provide additional information regarding this particular process which is used for separation of $CO_2/N_2$ mixture.

**Table S3.** Additional input parameters for simulation of the VSA-LPP process

| **Input parameters** | |
|---|---|
| **Inlet feed conditions** | |
| Feed composition | 15% $CO_2$ + 85% $N_2$ |
| Feed temperature (K) | 298.15 |
| **Column specifications** | |
| Wall (ambient) temperature (K) | 298.15 |
| Column length (m) | 1.0 |
| Inner column radius (m) | 0.1445 |
| Outer column radius (m) | 0.1620 |
| Column void fraction | 0.37 |
| Specific heat capacity of column wall (J/kg·K) | 537 |
| Density of column wall (kg/m$^3$) | 7800 |
| Wall heat transfer co-efficient (J/m$^2$·K·s) | 59.1 |
| Outside heat transfer co-coefficient (J/m$^2$.K.s) | 0.0 (column wall to oven) |
| **Simulation set-up** | |
| Numerical scheme | Finite volume, Van Leer flux limiter[14, 15] |
| Number of Finite volumes | 30.0 |
| Pressure drop model | Ergun |
| Conditions of cyclic steady state | 700 cycles / tolerance = $10^{-4}$ |
| **Adsorbent properties** | |
| **Cu-BTC** | |
| Tortuosity, τ (-) | $\tau = \begin{cases} 5.0 & \varepsilon_p < 0.2 \\ \frac{1}{\varepsilon_p} & 0.2 < \varepsilon_p < 0.8 \\ 1.25 & \varepsilon_p > 0.8 \end{cases}$ |
| Crystal density (kg/m$^3$) | 879.10 |
| Specific heat capacity of adsorbent (J/kg·K) | 1457[16, 17] |
| Molecular diffusivity (m$^2$/s) | $1.28\times10^{-5}$ |
| Knudsen diffusivity for $CO_2$ (m$^2$/s) | $4.67\times10^{-5}$ |
| Knudsen diffusivity for $N_2$ (m$^2$/s) | $5.85\times10^{-5}$ |
| **MOF74-Ni** | |
| Tortuosity (τ) | $\tau = \begin{cases} 5.0 & \varepsilon_p < 0.2 \\ \frac{1}{\varepsilon_p} & 0.2 < \varepsilon_p < 0.8 \\ 1.25 & \varepsilon_p > 0.8 \end{cases}$ |
| Crystal density (kg/m$^3$) | 1166.97 |
| Specific heat capacity of adsorbent (J/kg·K) | 1100[18]* |

| | |
|---|---|
| Molecular diffusivity ($m^2/s$) | $1.28\times10^{-5}$ |
| Knudsen diffusivity for $CO_2$ ($m^2/s$) | $2.02\times10^{-5}$ |
| Knudsen diffusivity for $N_2$ ($m^2/s$) | $2.53\times10^{-5}$ |
| **Silicalite (MFI)** | |
| Tortuosity (τ) | $\tau = \begin{cases} 5.0 & \varepsilon_p < 0.2 \\ \frac{1}{\varepsilon_p} & 0.2 < \varepsilon_p < 0.8 \\ 1.25 & \varepsilon_p > 0.8 \end{cases}$ |
| Crystal density ($kg/m^3$) | 1837.96 |
| Specific heat capacity of adsorbent (J/kg·K) | 771[19] |
| Molecular diffusivity ($m^2/s$) | $1.28\times10^{-5}$ |
| Knudsen diffusivity for $CO_2$ ($m^2/s$) | $1.50\times10^{-5}$ |
| Knudsen diffusivity for $N_2$ ($m^2/s$) | $1.88\times10^{-5}$ |
| **Zeolite 13X** | |
| Tortuosity (τ) | $\tau = \begin{cases} 5.0 & \varepsilon_p < 0.2 \\ \frac{1}{\varepsilon_p} & 0.2 < \varepsilon_p < 0.8 \\ 1.25 & \varepsilon_p > 0.8 \end{cases}$ |
| Crystal density ($kg/m^3$) | 1413.82 |
| Specific heat capacity of adsorbent (J/kg·K) | 920[20] |
| Molecular diffusivity ($m^2/s$) | $1.28\times10^{-5}$ |
| Knudsen diffusivity for $CO_2$ ($m^2/s$) | $7.42\times10^{-5}$ |
| Knudsen diffusivity for $N_2$ ($m^2/s$) | $9.30\times10^{-5}$ |

* Specific heat capacity of pelletized MOF74-Ni measured by Krishnamurthy et al.[18] using the thermogravimetric differential scanning calorimetry (TGA-DSC) method. We obtained this information through direct communication with the authors, although they have not reported this value in their recent publication.

## 4. Dual-Site Langmuir Fitting

We have used the dual-site Langmuir (DSL) adsorption model to fit the adsorption data obtained from GCMC simulations. All GCMC-simulated adsorption isotherms are scaled down by 20% to account for weight fraction of binder in pelletized samples. The resulting fitting parameters are provided in Table S4.

**Table S4**: DSL parameters of pure component adsorption isotherms

| **Cu-BTC** | | | **MOF74-Ni** | | |
|---|---|---|---|---|---|
| | **$CO_2$** | **$N_2$** | | **$CO_2$** | **$N_2$** |
| $q_{s1}$ (mmol/g) | 0.25 | 0.25 | $q_{s1}$ (mmol/g) | 9.86 | 9.86 |
| $b_{01}$ ($bar^{-1}$) | 9.44E-5 | 8.04E-5 | $b_{01}$ ($bar^{-1}$) | 1.03E-05 | 1.77E-04 |
| $-\Delta H_1$ (J/mol) | 28344.26 | 20692.11 | $-\Delta H_1$ (J/mol) | 31034.64 | 11396.82 |
| $q_{s2}$ (mmol/g) | 26.27 | 26.27 | $q_{s2}$ (mmol/g) | 1.96E-11 | 1.96E-11 |
| $b_{02}$ ($bar^{-1}$) | 6.02E-6 | 7.46E-5 | $b_{02}$ ($bar^{-1}$) | 0.00 | 1.77E-04 |
| $-\Delta H_2$ (J/mol) | 25399.95 | 11659.46 | $-\Delta H_2$ (J/mol) | 0.00 | 11396.82 |

| Silicalite-1 | | | Zeolite 13X | | |
|---|---|---|---|---|---|
| | **$CO_2$** | **$N_2$** | | **$CO_2$** | **$N_2$** |
| $q_{s1}$ (mmol/g) | 1.57 | 1.57 | $q_{s1}$ (mmol/g) | 3.16 | 3.16 |
| $b_{01}$ ($bar^{-1}$) | 2.37E-05 | 1.00E-04 | $b_{01}$ ($bar^{-1}$) | 9.23E-07 | 5.85E-05 |
| $-\Delta H_1$ (J/mol) | 26813.84 | 16009.49 | $-\Delta H_1$ (J/mol) | 47612.86 | 16059.73 |
| $q_{s2}$ (mmol/g) | 1.16 | 1.16 | $q_{s2}$ (mmol/g) | 2.24 | 2.24 |
| $b_{02}$ ($bar^{-1}$) | 1.94E-05 | 1.00E-04 | $b_{02}$ ($bar^{-1}$) | 4.88E-07 | 5.85E-05 |
| $-\Delta H_2$ (J/mol) | 27302.67 | 16009.49 | $-\Delta H_2$ (J/mol) | 38545.63 | 16059.73 |

The fitting is performed following a protocol explained in our previous publication[21]. For MOF74-Ni, Silicalite-1 and Zeolite 13X, we have adopted "fitting procedure 3" where $b_{o1,N2} = b_{o2,N2}$ constraint is applied for fitting $N_2$ isotherms using the DSL model given by

$$q_i^* = \sum_{j=1}^{2}\left[q_{j,i}^s \frac{b_{j,i} \times P}{1 + b_{j,i} \times P}\right] \quad (1)$$

here, $q_{j,i}^s$is saturation capacity of site $j$ with respect to species $i$. $b_{j,i}$ is affinity of each site described by the van't Hoff equation defined by

$$b_{j,i} = b_{oj,i} \exp\left(\frac{-\Delta H_{j,i}}{RT}\right) \quad (2)$$

For Cu-BTC however, a reasonable fit couldn not be obtained under the constraint $b_{o1,N2} = b_{o2,N2}$. Therefore, $N_2$ adsorption isotherms were simulated up to 5 bar at various temperatures where curvature of isotherms would allow us to relax the above fitting constraint to $b_{o1,N2} \geq b_{o2,N2}$. High-pressure GCMC adsorption isotherms of $N_2$ in Cu-BTC is provided in Fig S1.

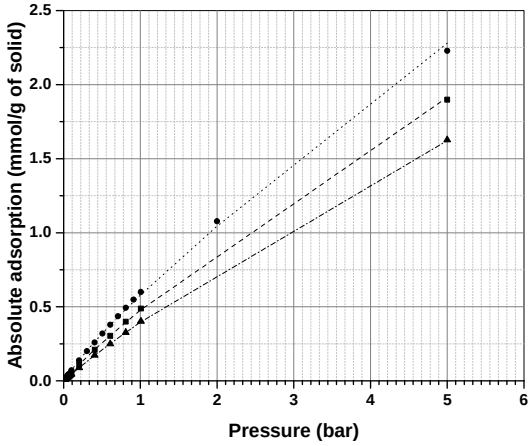

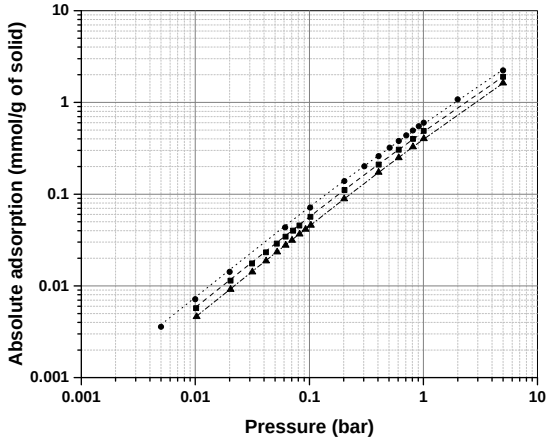


**Fig S1.** High pressure adsorption isotherms of $N_2$ in Cu-BTC obtained from GCMC simulations in linear (top) and logarithmic (bottom) scales. Circle, square and triangle symbols represent adsorption isotherms at 258.15 K, 268.15 K and 278.15 K respectively.

## 5. Adsorption isotherm of $N_2$ in MOF74-Ni

As mentioned in Section (3.1) of the main article, our GCMC simulations largely underestimate experimental adsorption isotherms of $N_2$ in MOF74-Ni. The reason for this is inadequacy of currently available generic force fields in molecular simulations which are not optimized for MOFs with coordinatively unsaturated metal sites as explained in Section (2.1) of the main article. To illustrate the extent by which experimental isotherms are underestimated, we compare GCMC simulated adsorption isotherms of $N_2$ by the experimental data recently published by Krishnamurthy et al.[18].

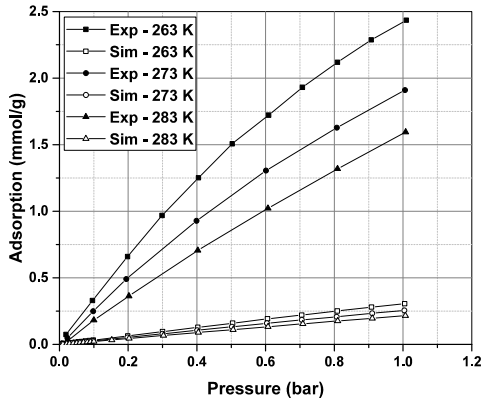


**Fig S2.** GCMC-simulated adsorption isotherms of $N_2$ in MOF74-Ni from this study (open symbols) compared to the experimental isotherms reported by Krishnamurthy et al[18] (closed symbols).

## 6. Distribution of pellet size and pellet porosity

Distributions of pellet diameter and pellet porosity across Pareto fronts of each individual material are illustrated in Fig S3 and Fig S4:

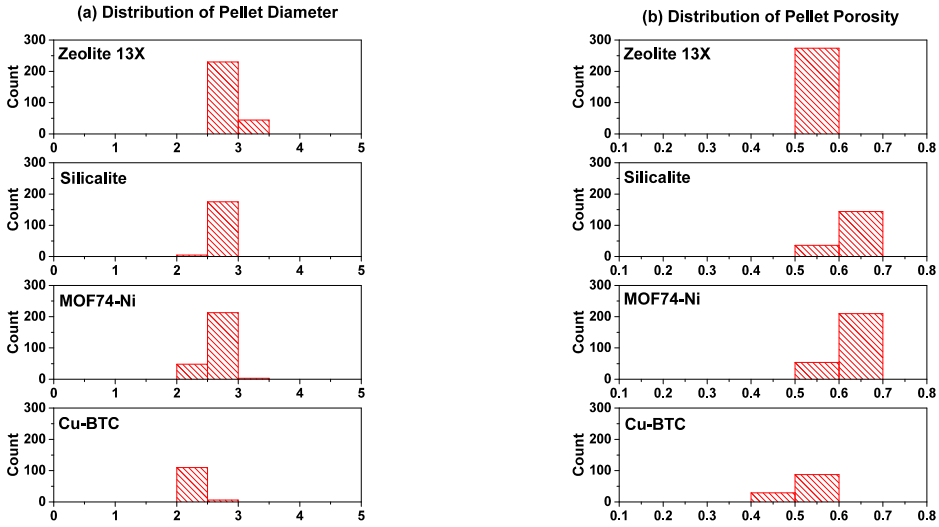


**Fig S3.** Distribution of pellet size (a) and pellet porosity (b) across Pareto fronts of each individual material corresponding to Fig 11 of the main article.

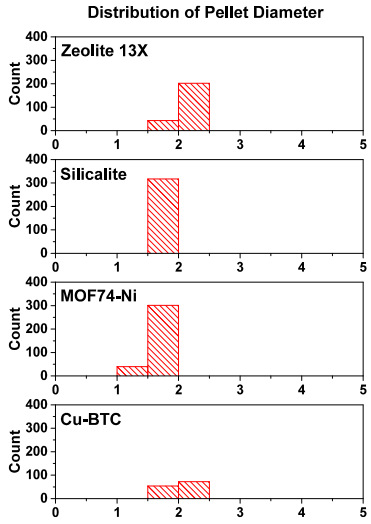


**Fig S4.** Distribution of pellet size across Pareto fronts of each individual material corresponding to Fig 13 of the main article.

## 7. Variation of other decision variables

Similar to Fig 11 of the main article where variation of pellet size and pellet porosity across Pareto fronts of the four adsorbent materials are illustrated, here we show how other decision variables of the 4-step VSA-LPP process change across Pareto front of each material for the case corresponding to Fig 11.

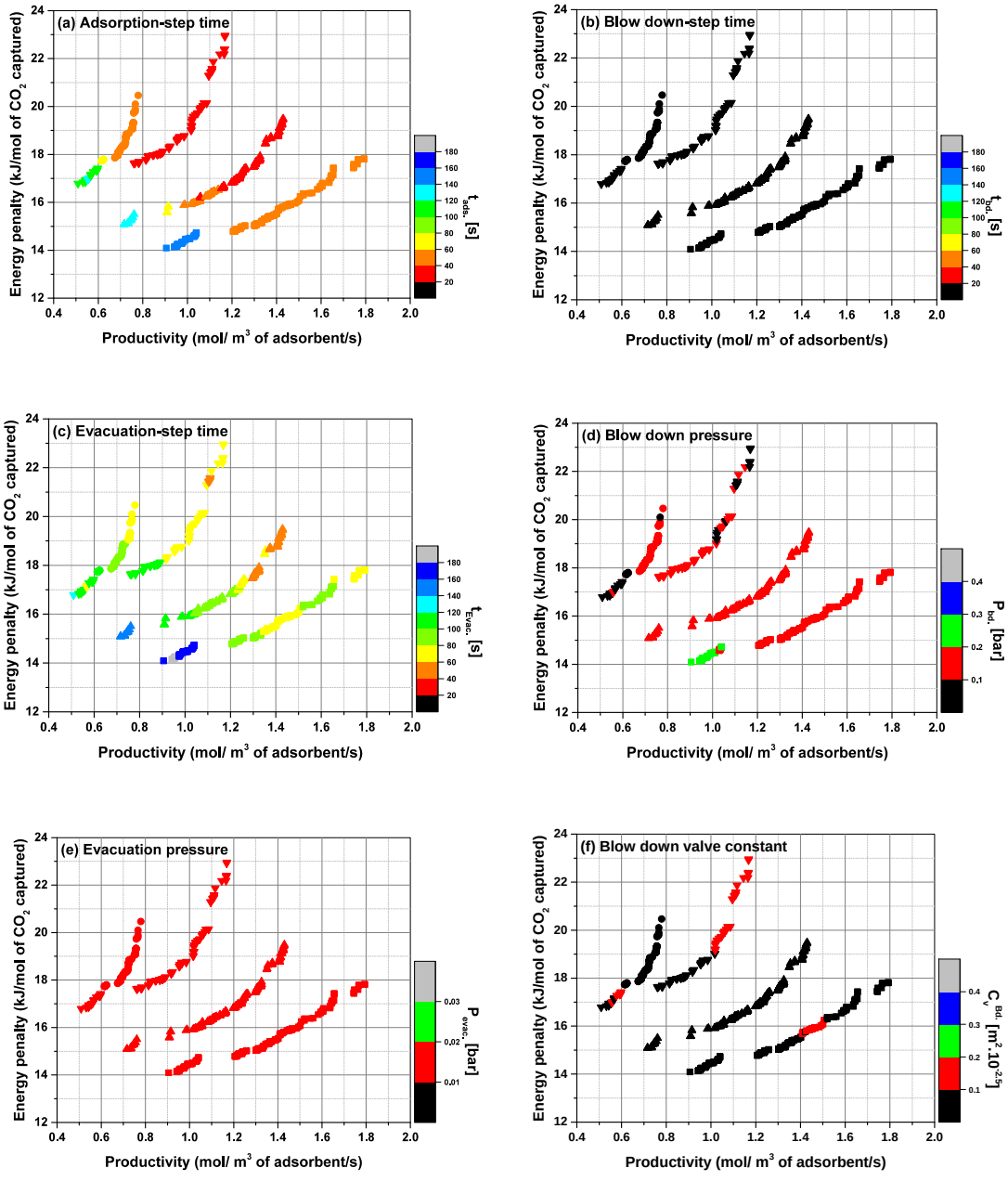

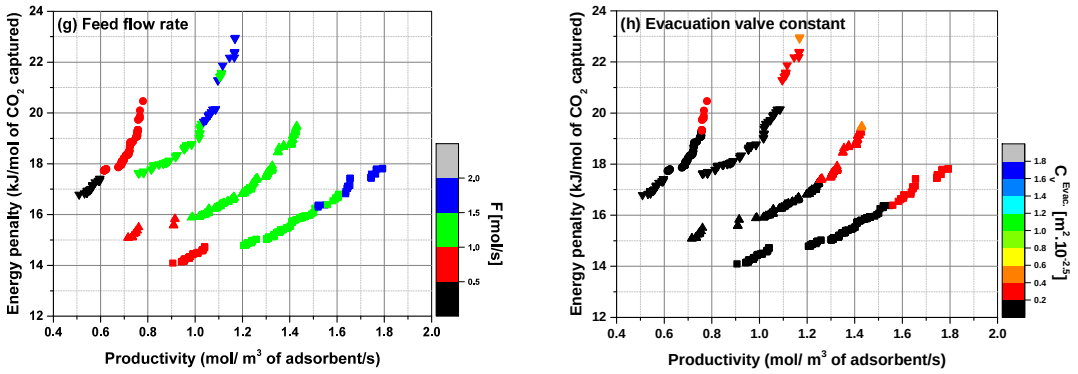


**Fig S5.** Variation of all decision variables (except pellet diameter and pellet porosity) across Pareto fronts of Cu-BTC (down-pointing triangle), MOF74-Ni (square), Silicalite-1 (circle) and Zeolite 13X (up-pointing triangle) for the case presented in Fig 11 of the main article.

## 8. Working capacity of the VSA-LPP cycle on the Pareto fronts

This section provides results of our detailed analyses on working capacity of various data points located on Pareto fronts of each material. Table S5 lists working capacity and ratio of $\frac{\Delta q}{\Delta c}$ for three points on Pareto fronts of each material corresponding to their minimum, median and maximum productivity values.

As discussed in Section (3.5) of the main article, our analyses show that cycle optimization drives the process to operate on some portions of the isotherm with lower curvature (non-linearity), which leads to lower than expected working capacities during a single cycle. This is evident in Table S5 where calculated working capacities of all materials correspond to a narrow band on the adsorption isotherm along which the isotherm has lower curvature.

**Table S5.** Working capacity and secant of $CO_2$ adsorption isotherm for various points located on the Pareto fronts of each material

| index | Material | Productivity (mol $CO_2$/$m^3$ of solid/s) | Energy Penalty (kJ/mol of $CO_2$) | Working capacity ($\Delta q$) (mol/$m^3$ of solid) | $\frac{\Delta q}{\Delta c}$ (-) |
|---|---|---|---|---|---|
| 1 | Zeolite 13X | 0.72 | 15.09 | 218.69 | 105.93 |
| 2 | Zeolite 13X | 1.02 | 15.92 | 176.81 | 92.36 |
| 3 | Zeolite 13X | 1.43 | 19.49 | 177.91 | 94.19 |
| 4 | Cu-BTC | 0.51 | 16.79 | 137.05 | 91.98 |
| 5 | Cu-BTC | 0.85 | 17.97 | 144.93 | 71.67 |
| 6 | Cu-BTC | 1.17 | 22.96 | 135.94 | 74.84 |
| 7 | MOF74-Ni | 0.91 | 14.09 | 318.09 | 176.38 |
| 8 | MOF74-Ni | 1.35 | 15.32 | 210.57 | 138.77 |
| 9 | MOF74-Ni | 1.79 | 17.82 | 256.71 | 144.65 |
| 10 | Silicalite-1 | 0.61 | 17.73 | 123.65 | 65.46 |

| | | | | | |
|---|---|---|---|---|---|
| 11 | Silicalite-1 | 0.70 | 18.13 | 128.08 | 65.29 |
| 12 | Silicalite-1 | 0.78 | 20.47 | 127.42 | 65.42 |

To better demonstrate this finding, we focus on one example case and explain it in detail knowing that all other cases follow the same trend. For this, we choose the second Pareto point for Zeolite 13X as provided in Table S5, where productivity and energy penalty are equal to 1.02 mol/m$^3$/s and 15.92 kJ/mol respectively. For this point, temperature and concentration profiles of $CO_2$ are provided in Fig S6.

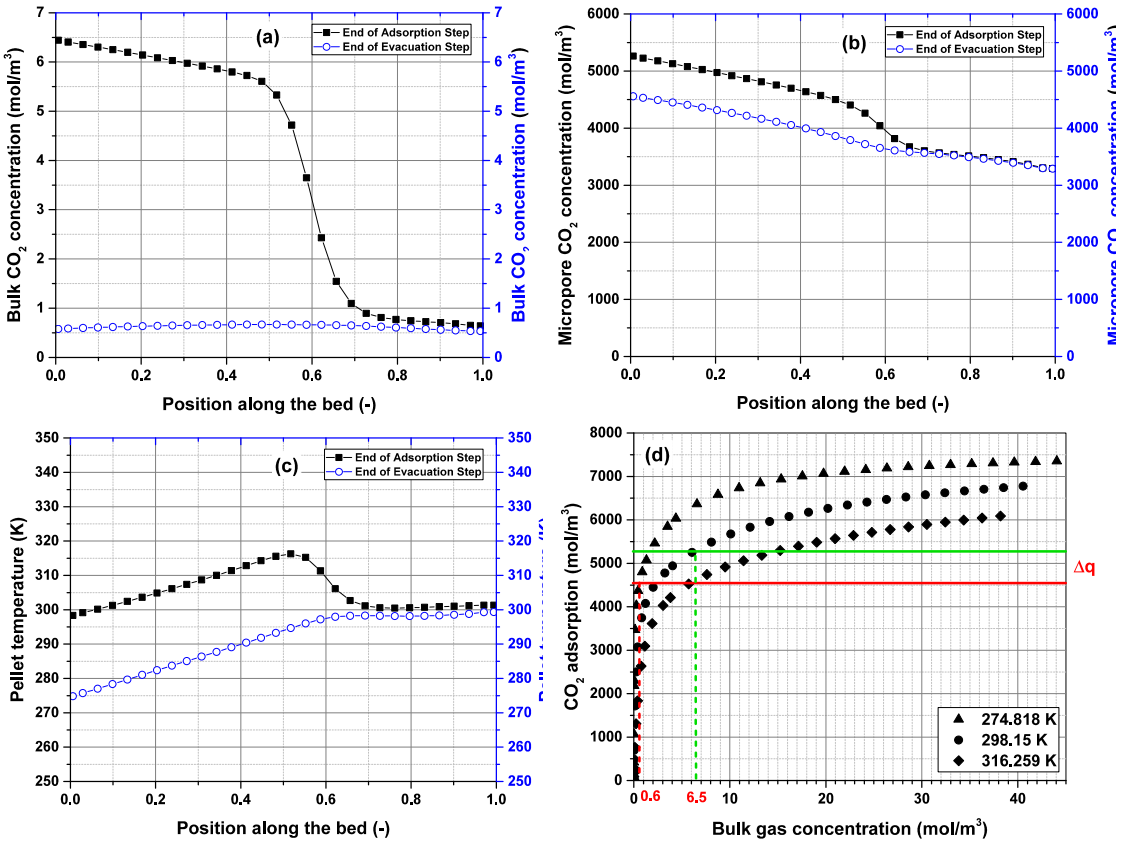


**Fig S6.** Bulk concentration profiles of $CO_2$ (a) micropore concentration profiles of $CO_2$ (b), temperature profiles of the bed (c), and single-component adsorption isotherms of $CO_2$ at various temperatures (d). The information provided in this figure corresponds to the second Pareto point of Zeolite 13X listed in Table S5.

For the illustration purpose, we focus on the starting point of the bed and identify $CO_2$ micropore concentration at the end of adsorption and evacuation steps. The difference between the amounts of $CO_2$ adsorbed at these two cycle times corresponds to the working capacity of the cycle on the starting point of the bed.

According to Fig S6 (c), temperature is ~298 K at the end of adsorption step; hence the desired adsorption point is located on the isotherm shown by circular symbols in Fig S6 (d). To exactly

locate this point on the adsorption isotherm, the corresponding bulk concentration of $CO_2$ at this temperature must be identified which is given by Fig S6 (a) and is equal to 6.5 mol/m$^3$ at the beginning of the bed. Given both bulk concentration and temperature are now identified, position of the desired adsorption point on the isotherm can be determined. This corresponds to ~5250 mol/m$^3$ which is marked by a green horizontal line in Fig S6 (d). Interestingly, micropore concentration of $CO_2$ at the beginning of the bed is also equal to 5263 mol/m$^3$ according to Fig S6 (b), an indication of the VSA process operating very close to an equilibrium cycle.

In a similar fashion, position of desorption point at the beginning of the bed can be determined on an isotherm. According to Fig S6 (c), desorption occurs at ~275 K at this point of the bed. Moreover, Fig S6 (a) provides bulk concentration of $CO_2$ at this point which is equal 0.6 mol/m$^3$. From this information, position of the equilibrium desorption point (marked by red horizontal line) can be identified on the isotherm illustrated by triangular symbols (~4500 mol/m$^3$) in Fig S6 (d). This number is very close to micropore concentration of $CO_2$ at the end of evacuation step as shown in Fig S6 (b) whose exact value is 4559 mol/m$^3$. Again, this is an indication of the VSA cycle operating close to equilibrium cycle conditions.

The difference observed between adsorbed concentration of $CO_2$ at the end of adsorption and evacuation steps (the illustrated band between red and green horizontal lines) is working capacity of the cycle for a point located at the beginning of the bed, which is equal to $\Delta q = 5263 - 4559 = 704$ mol/m$^3$. Clearly, this number is different with actual working capacity of the bed which is calculated by integrating total adsorption along the entire bed taking into account both micro- and macropore concentration of $CO_2$. The correct working capacity of the cycle is provided in Table S5, nevertheless the illustration adopted above helps us to explain how the cycle optimization drives the process to operate on some portions of the isotherm with lower non-linearity, and why this leads to lower than expected working capacities during a single cycle. The working capacity calculated above (704 mol/m$^3$) is ~10 times smaller than maximum capacity of the adsorbent at 1 bar (40.55 mol/m$^3$) at 298 K which is about 7000 mol/m$^3$ according to the isotherm shown Fig S6 (d). Such a small working capacity explains lower non-linearity of the cycle operation curve compared to non-linearity of the overall adsorption isotherm. The small working capacity of the 4-step VSA cycle observed in our study is a result of low partial pressure of $CO_2$ (i.e. 0.15 bar), the drop of temperature from 298 K to 275 K from adsorption to desorption in the non-isothermal VSA model, and the fact that only

60% of the bed is actually used for adsorption. The latter is a direct impact of the 90% $CO_2$ recovery requirement (i.e. constraint) during cycle optimization.

## 9. Distribution of dimensionless parameter "$\alpha$"

Distributions of dimensionless parameter $\alpha$ for the entire configurations simulated during process optimization of each individual material (corresponding to Fig 15 (a), (c), (e) and (g) of the main article) are illustrated in the Fig S7.

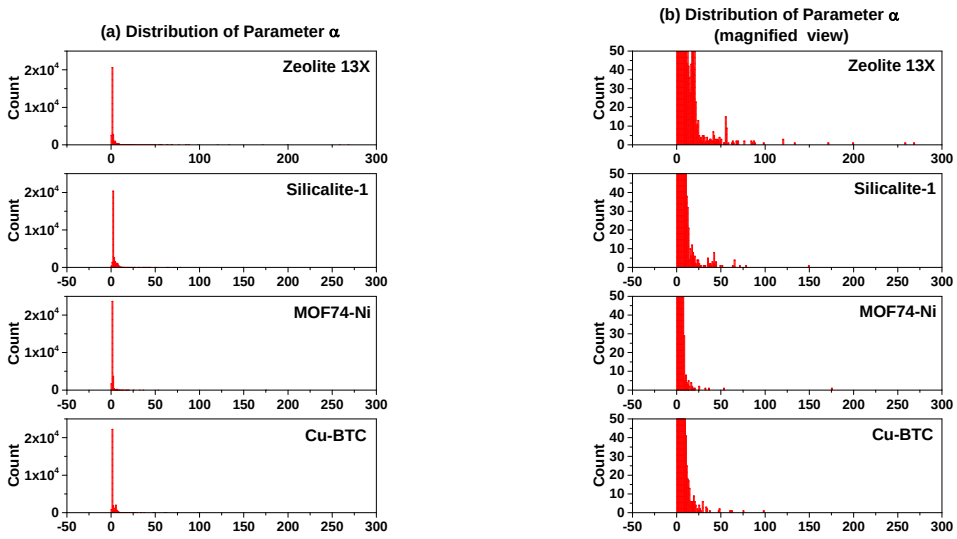


**Fig S7.** Distribution of dimensionless parameter $\alpha$ across all process configurations of the individual materials (a), magnified view of the left plot (b)

## References


1. S. S. Y. Chui, S. M. F. Lo, J. P. H. Charmant, A. G. Orpen and I. D. Williams, *Science*, 1999, **283**, 1148.
2. Q. Yang and C. Zhong, *ChemPhysChem*, 2006, **7**, 1417-1421.
3. J. J. Potoff and J. I. Siepmann, *AIChE Journal*, 2001, **47**, 1676-1682.
4. J. R. Karra and K. S. Walton, *Langmuir*, 2008, **24**, 8620-8626.
5. K. Lee, J. D. Howe, L.-C. Lin, B. Smit and J. B. Neaton, *Chemistry of Materials*, 2015, **27**, 668-678.
6. R. Mercado, B. Vlaisavljevich, L.-C. Lin, K. Lee, Y. Lee, J. A. Mason, D. J. Xiao, M. I. Gonzalez, M. T. Kapelewski, J. B. Neaton and B. Smit, *The Journal of Physical Chemistry C*, 2016, **120**, 12590-12604.
7. J. G. Harris and K. H. Yung, *The Journal of Physical Chemistry*, 1995, **99**, 12021-12024.
8. K. Makrodimitris, G. K. Papadopoulos and D. N. Theodorou, *The Journal of Physical Chemistry B*, 2001, **105**, 777-788.
9. A. K. Rappe, C. J. Casewit, K. S. Colwell, W. A. Goddard and W. M. Skiff, *Journal of the American Chemical Society*, 1992, **114**, 10024-10035.
10. M. Fischer and R. G. Bell, *The Journal of Physical Chemistry C*, 2012, **116**, 26449-26463.
11. D. H. Olson, *Zeolites*, 1995, **15**, 439-443.
12. V. Bojan and P. L. Alexander, *Modelling and Simulation in Materials Science and Engineering*, 2016, **24**, 045002.
13. C. S. Murthy, K. Singer, M. L. Klein and I. R. McDonald, *Molecular Physics*, 1980, **41**, 1387-1399.
14. B. van Leer, *Journal of Computational Physics*, 1974, **14**, 361-370.
15. J. MacKinnon Robert and F. Carey Graham, *International Journal for Numerical Methods in Fluids*, 2002, **41**, 151-183.
16. B. Silva, I. Solomon, A. M. Ribeiro, U. H. Lee, Y. K. Hwang, J.-S. Chang, J. M. Loureiro and A. E. Rodrigues, *Separation and Purification Technology*, 2013, **118**, 744-756.
17. M. G. Plaza, A. M. Ribeiro, A. Ferreira, J. C. Santos, U. H. Lee, J.-S. Chang, J. M. Loureiro and A. E. Rodrigues, *Separation and Purification Technology*, 2012, **90**, 109-119.
18. S. Krishnamurthy, R. Blom, M. C. Ferrari and S. Brandani, *Adsorption*, 2019, DOI: 10.1007/s10450-019-00162-x.
19. G. K. Johnson, I. R. Tasker, D. A. Howell and J. V. Smith, *The Journal of Chemical Thermodynamics*, 1987, **19**, 617-632.
20. D. Schawe, Doctor of Engineering (Dr. Ing.), University of Stuttgart, 2001.
21. A. H. Farmahini, S. Krishnamurthy, D. Friedrich, S. Brandani and L. Sarkisov, *Industrial & Engineering Chemistry Research*, 2018, **57**, 15491-15511.